

# Experimental results with a second-generation Roddier & Roddier phase mask coronagraph

M. N'Diaye<sup>1,2</sup>, K. Dohlen<sup>1</sup>, S. Cuevas<sup>2</sup>, P. Lanzoni<sup>1</sup>, F. Chemla<sup>3</sup>, C. Chaumont<sup>3</sup>, R. Soummer<sup>4</sup>, and E. T. Griffiths<sup>5</sup>

<sup>1</sup> Laboratoire d'Astrophysique de Marseille, UMR6110, OAMP, CNRS/Université de Provence, 38 rue Frédéric Joliot-Curie, 13388 Marseille Cedex 13, France

e-mail: mndiaye@astroscu.unam.mx; Kjetil.Dohlen@oamp.fr

<sup>2</sup> Instituto de Astronomía, Universidad Nacional Autónoma de México, Apartado Postal 70-264 Ciudad Universitaria, 04510 México D.F., Mexico

e-mail: chavoc@astroscu.unam.mx

<sup>3</sup> GEPI, Observatoire de Paris, 5 Place Jules Janssen, 92195 Meudon Cedex, France

e-mail: fanny.chemla@obspm.fr

<sup>4</sup> Space Telescope Science Institute, 3700 San Martin Drive, Baltimore, MD 21218, USA

e-mail: soummer@stsci.edu

<sup>5</sup> American Museum of Natural History, 79th Street at Central Park West, New York, NY 10024, USA

Received 19 February 2009 / Accepted 28 September 2009

## ABSTRACT

**Context.** Coronagraphic techniques are required to observe substellar mass companions close to nearby bright stars by direct imagery. Phase mask coronagraphs are particularly interesting because they give access to the innermost regions. While the principle of the first such concept was validated experimentally a decade ago, the achieved brightness attenuation was too low to be conclusive, probably due to the imperfect thickness profile of the mask.

**Aims.** We have manufactured and tested a second-generation Roddier & Roddier coronagraph in preparation for the development of more elaborate phase mask designs, planned to be used in the future European Extremely Large Telescope.

**Methods.** A monolithic phase mask was made by ion beam machining. Experimentally obtained coronagraphic images were compared with simulated images.

**Results.** Good agreement with theory was obtained. A peak attenuation of 216 was achieved, and a contrast of  $\sim 10^{-5}$  was measured at  $5.7 \lambda/D$ . The results exploring contrasts obtained at different distances from the star for different mask dimensions are particularly interesting, confirming predictions made in the literature.

**Key words.** instrumentation: high angular resolution – techniques: high angular resolution – telescopes – methods: laboratory

## 1. Introduction

Direct detection and imagery of faint stellar companions, like extrasolar planets or brown dwarfs, are some of the most exciting challenges of contemporary observational astrophysics. Such imagery will in particular give access to spectral analysis of the emitted or reflected light from these objects, providing data about atmospheric composition. The detection and quantification of bio-signals (like water [H<sub>2</sub>O], oxygen [O<sub>2</sub>], ozone [O<sub>3</sub>]...) will bring elements of response about the possible presence of life (Woolf & Angel 1998). With images of faint companions, it will also be possible to better understand mechanisms of planet formation (Burrows & Sharp 1999) and calibrate the current atmospheric evolution models (Marley et al. 1999). However, planetary stellar companions are predicted to be very faint compared to their host star; reduction of the diffracted star light by the aid of coronagraphic devices is therefore required.

Roddier & Roddier (1997) proposed a new coronagraphic concept based on replacing the usual opaque occulting disk with a small transparent phase mask, referred to as the Roddier and Roddier phase mask (RRPM). They showed that if the central core of the stellar diffraction pattern was delayed by a  $\pi$  phase change, then destructive interference occurred within the pupil, displacing virtually all of the starlight into a halo surrounding the

geometric pupil image. Removing this energy with a Lyot stop in the subsequent pupil plane was shown to lead to an important reduction of diffracted starlight in the final image projected onto the detector or into a spectrographic instrument.

The action of the phase mask can be understood intuitively by considering the electric field in the image plane, consisting of a peak surrounded by positive and negative rings. By the Fourier integral theorem (e.g., see Goodman 1996), the integral of this function over the entire image plane equals the electric field strength at the center of the pupil. We can find a radius  $r_1$  such that the integral inside this radius equals the integral outside of this radius. By applying a  $\pi$  phase shifting mask of this radius centered on the star in the focal plane, so that the electric field within the mask is inverted, the integrated electric field, hence the field strength at the center of the pupil, will become zero.

The complex electric field just after the coronagraph mask  $e$  can be written

$$e = e_0(1 - 2m) = e_0 - e_1, \quad (1)$$

where  $e_0$  is the electric field just before the mask,  $m$  is a top-hat function equal to unity within radius  $r_1$  and zero outside of this radius, and  $e_1 = 2me_0$ . The resulting field distribution in the following pupil plane is the difference between the original pupil,  $E_0$  (letting capital letters represent the Fourier transform

of lower case letters), and  $E_1$ , the Fourier transform of  $e_1$ . Since  $e_1$  is a bounded function of width smaller than the central lobe of  $e_0$ , its Fourier transform is a bell-shaped function somewhat wider than  $E_0$ . For the value of  $r_1$  determined above, the central value of  $E_1$  equals that of  $E_0$ , giving zero at the center of the coronagraphic exit pupil,  $E = E_0 - E_1$ . The resultant function increases towards the edge of the geometrical pupil, where a sharp discontinuity occurs, giving rise to negative electric field strength outside of the pupil. Since the action of the coronagraph only applies to the central object, any field object is transmitted normally through the geometric pupil. No loss of useful signal is therefore suffered by placing an opaque mask with a hole equal to the geometrical pupil, i.e. a Lyot stop, in this pupil plane.

The distribution of the residual electric field within the pupil can be adjusted by adjusting the mask size. Increasing  $r_1$  slightly results in an increase in the function  $E_1$  within the pupil, allowing us to adjust the integral within the Lyot stop to become zero. Again invoking the Fourier integral theorem, this results in perfect nulling of the central peak in the final coronagraphic image. A further increase in  $r_1$  allows a perfect equalization of the two functions at the edge of the pupil, so that the residual energy distribution in the exit pupil falls off smoothly towards zero, i.e. simulating an apodized pupil.

The explanation offered above uses the term *interferometric* or *nulling* to describe this phase-mask coronagraph: the residual electric field is indeed a subtraction, i.e. destructive interference between two fields, the original object field and the field diffracted by the phase mask. We also note that such phase masks are equivalent to Mach-Zehnder interferometers with amplitude and/or phase masks inserted in the interfering arms, as discussed by Dohlen (2004).

In 1998, Roddier and Roddier, with co-investigators from the Institute for Astronomy of the University of Hawaii, joined forces with colleagues at the Universidad Nacional Autónoma de México (UNAM), including one of us (SC), in order to realize the first RRPM and to test the theoretical predictions experimentally. This first-generation phase mask was made by photolithographic deposition of an appropriately sized spot of SiO<sub>2</sub> of thickness 700 nm and diameter 200  $\mu\text{m}$ .

While the results of this experiment, described in detail in Guyon et al. (1999), clearly validated the principles of this new coronagraphic concept, it achieved only a modest peak intensity attenuation of 16. Theoretically, carefully adjusting the size of the mask to the size of the diffraction pattern (or vice-versa, by the aid of a variable iris entrance pupil), a peak intensity attenuation of infinity could have been achieved.

The modest attenuation achieved was explained by the rounded edges of this first-generation mask. It was therefore clear that technological improvements would be required to push this concept further. This conclusion, together with the double chromatism suffered by the RRPM, both in terms of phase delay and lateral dimension, made the concept sufficiently unattractive to remain virtually unexplored in the literature since then. It did open the road for other phase mask concepts, however, in particular the four-quadrant phase mask (FQPM, Rouan et al. 2000) which has been extensively studied (Riaud et al. 2001) and tested (Riaud et al. 2003; Mawet et al. 2006) and which currently equips high-contrast imaging projects on the ground (Boccaletti et al. 2004; Gratadour et al. 2005) and, soon, in space (Baudoz et al. 2006). It also spurred the development of a phase-mask coronagraph more directly related to the RRPM, the dual-zone phase mask (DZPM, Soummer et al. 2003b). This concept is based on a small structure covering the central core of the stellar diffraction pattern, but instead of a single phase retardation,

this mask includes a second, annular phase retarder surrounding the Roddier-style cylindrical phase disk. None of the retardations being  $\pi$ , achromatic destructive interference is reached by a three-vector nulling, rather than a two-vector nulling as in the original RRPM concept.

An important difference between the circular phase mask, Roddier-type coronagraphs and the four-quadrant phase mask coronagraphs is their tolerance to non-circular or centrally obstructed pupils. It can be understood from the intuitive description given above that in the former case, the function  $E_1$  remains a smooth bell-shaped function whatever the shape of  $E_0$ , and so, when the optimal size of the mask has been determined, the field in the exit pupil will remain small within the geometrical pupil and bright outside of this limit and within any obscuration (shadow of the secondary mirror and spiders, gaps between segments, etc.). In the case of the FQPM and related designs, light is rejected to the outside of any circular edge. Since an obstructed aperture can be seen as the subtraction of two circular pupils, the negative electric field contained within the central obscuration will therefore be recovered within the geometrical aperture in the exit pupil plane.

Thanks to its large potential for wide-band coronagraphy and its advantage with respect to pupil obscurations, the DZPM concept has been preselected as a candidate for the EPICS planet finder instrument (Kasper et al. 2008) for the European Extremely Large Telescope (E-ELT). In this context, a proof of concept experiment has been initiated in the framework of the European Union FP7 program. In preparation for this work, and in order to test the improvements during the last decade of the capacity of micro-optics technology to produce straight-edged phase structures, we decided to repeat the test of the RRPM using a new, second-generation, phase mask. The results of this experiment are reported in this paper. In Sect. 2, we describe the design of this new mask and the technology with which it was manufactured. In Sect. 3, we describe the experimental setup and measurement protocol and in Sect. 4, we present results of the experiments.

We do not consider in this paper the performance of stellar coronagraphs in the presence of aberrations, although aberrations in the experimental setup are invoked as a possible explanation for some of the effects observed. In particular, it is well known that aberrations due to atmospheric turbulence are devastating to any attempt of stellar coronagraphy unless powerful adaptive optics correction is adopted (Racine et al. 1999; Sivaramakrishnan et al. 2001; Aime & Soummer 2004). Considering coronagraphic performance in the case of ideal optics allows us to evaluate the ultimate performance of a coronagraph, performance which could expectedly be approached in the forthcoming generation of exoplanet direct imaging systems, like SPHERE (Beuzit et al. 2006), GPI (Macintosh et al. 2006), HiCIAO (Hodapp et al. 2008), EPICS (Kasper et al. 2008), TPF (Traub et al. 2007), etc.

## 2. Design and manufacture of the second-generation Roddier & Roddier phase mask

While the deposition of a cylindrical spot of SiO<sub>2</sub> on a fused silica substrate could be considered a good option for the RRPM, it was judged risky because an inevitable index difference between mask and substrate would lead to interference effects whose impact on the coronagraphic performance is difficult to model and predict. Also, edge effects due to the lift-off of the excess mask

material may be expected, as was probably the case in the first-generation mask. An alternative, monolithic option was therefore investigated, where the phase dot is machined into the substrate by the aid of photo-lithographic reactive ion etching. By this technique, the phase mask appears as a hole rather than a dimple, creating phase advancement rather than retardation. This modification is of no consequence to the concept, since the important feature is the phase difference of  $\pi$  between the outside and inside of the mask. We have already experimented with this approach in the context of the development of a Zernike phase contrast sensor dedicated to the measurement of phasing errors in segmented telescopes. The mask depth is in that case adjusted to give a phase change of  $\pi/2$  within the mask, so as to translate wavefront errors in the telescope pupil, and in particular those due to segment mis-alignment, into intensity variations (Dohlen et al. 2006). Although the dimensions and mask quality requirements were not the same in the two cases, the results were sufficiently good that the application of the same technology seemed reasonable.

The mask fabrication, carried out at the GEPI laboratory of the Observatory of Paris, included the following steps:

1. deposition of photoresist onto the substrate;
2. removal of a circular zone of photoresist corresponding to the mask dimension by UV photo-lithographic projection;
3. reactive ion etching of the substrate with SF<sub>6</sub> gas. Only the zone left naked by the photo-lithography is attacked;
4. cleaning of the substrate.

The duration of the etching process required to achieve the correct mask depth was determined by calibration, using a Veeco Dectac 8 stylus profilometer, see Fig. 1. The excellent shape of masks made by this procedure is evident from the profile, and further illustrated by scanning electronic microscopy (SEM), see Fig. 2. The root mean square (rms) roughness within the mask area is 0.8 nm, identical to that of the substrate outside of the mask. While a slight rounding of the edges can be seen, the transition zone is less than 1  $\mu\text{m}$  wide, corresponding to about 1% of the mask diameter. Compared with the estimated profile of the first generation mask presented in Guyon et al. (1999), for which the transition zone is seen to cover more than 40% of the diameter, the quality of our second-generation mask is truly extraordinary.

The optimal diameter of the RRPM was estimated by Roddier & Roddier (1997) to be about  $1.05 \lambda/D$ , corresponding to an integral of the electric field over the Lyot stop equal to zero, i.e. an infinite central peak attenuation. Recent research (Ferrari et al. 2007) shows that increasing the mask size to around  $1.5 \lambda/D$  leads to improved contrast in the surrounding halo, although the peak attenuation is reduced. To demonstrate this effect experimentally using a source of  $\lambda = 677 \text{ nm}$ , we designed our mask with a diameter of  $65 \mu\text{m}$ , allowing for a variable focal ratio of the coronagraphic bench ranging from  $F \sim 50$  to  $F \sim 100$ .

Mask thickness  $t$  is given by the equation:

$$(n - 1)t = \lambda/2, \quad (2)$$

where  $n$  is substrate refractive index. For fused silica,  $n = 1.46$ , and so the optimal mask depth was 740 nm.

### 3. Experimental setup

#### 3.1. Description of the assembly

The optical design of the coronagraphic assembly is shown in Fig. 3 top. The diode laser source is spatially filtered through

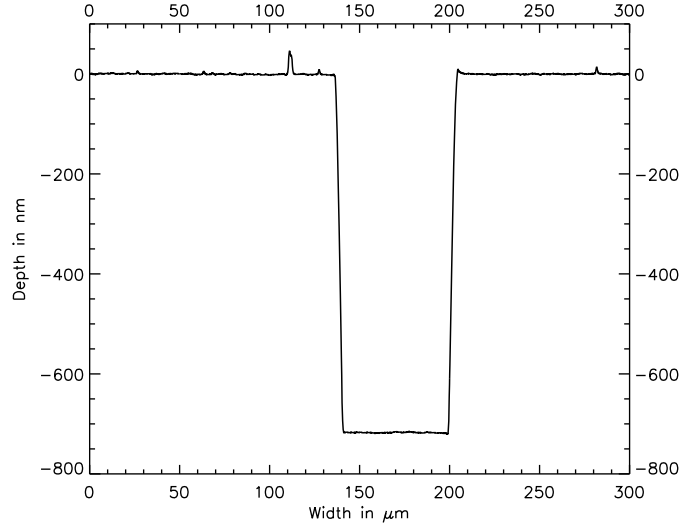


**Fig. 1.** Profile trace of the Roddier & Roddier phase mask measured by stylus profilometry.

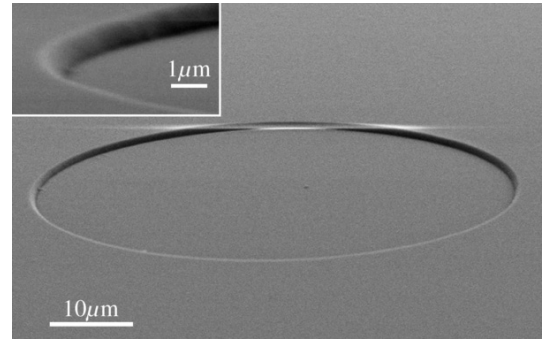


**Fig. 2.** Scanning electron microscope image of the Roddier & Roddier phase mask, showing real proportions of the full mask (main image) and a zoom on the edge (inset). The edge is remarkably well defined and the depth uniformity is virtually perfect. The images were obtained using an environmental scanning electron microscope, Extended Pressure-SEM (Zeiss Evo 60). To avoid the deposition of a metallic coating onto the component, which would have excluded its future use, we used the low-air pressure, or “environmental”, settings. The horizontal streak seen at the top of the mask is an artefact of the electron microscopy due to the accumulation of charges along the sharp edges of the mask, caused by the absence of a conductive coating.

a 5  $\mu\text{m}$  pinhole and collimated by the lens L1. A variable iris P1 defines the entrance pupil plane (A) of the system. To avoid excessive bench dimensions, a pupil size of 1–2 mm is used. We adjust the entrance pupil diameter, hence the dimension of the diffraction pattern projected onto the fixed mask, in order to change the relative mask diameter.

The lens L2 provides an image plane (B), in which the RRPM is placed, and also a pupil plane (C), in which the Lyot stop is located. While this setup appears ideal in the sense of minimizing optics, hence aberrations, it does not provide a telecentric beam to the coronagraph, but this does not appear to be of importance for this concept.

The following lens L3 projects the coronagraphic image (D) onto the camera. It also projects the pupil onto a plane (E) some 100 mm behind the image plane, allowing rapid switching between image and pupil plane observations by sliding the camera between these positions.

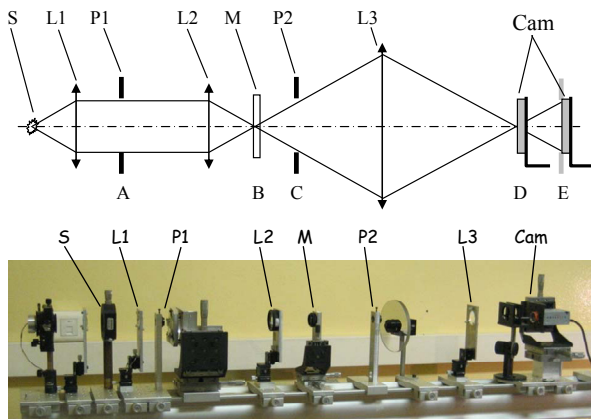


**Fig. 3.** Coronagraph experiment setup. S: source; L1: collimating lens; P1: variable diaphragm in the entrance pupil (plane A); L2: coronagraph lens; M: coronagraph mask (plane B); P2: variable diaphragm Lyot stop (plane C); L3: imaging lens; Cam: movable camera (planes D and E). *Top*: schematic representation of the experimental setup. Vertical scale is exaggerated for clarity. *Bottom*: photograph of the experimental setup.

The focal mask and Lyot stop are mounted on *xyz* micro-positioning stages, allowing both lateral and focus adjustment of these components. Once optimal positioning has been determined, the only adjustments necessary to perform the measurement protocol described below are a lateral ( $x$ ) movement of the mask to remove it or replace it on the stellar image (a displacement of a few 100  $\mu\text{m}$  is sufficient), and an adjustment of the diameter of the entrance pupil and the Lyot stop. A picture of the optical bench can be seen in Fig. 3 bottom.

Images were recorded using an 8-bit camera. To obtain an acceptable dynamic range, 3 images were taken at different exposure times from 0.04 ms to 1 s, and composite images were created by extracting annular zones from each image. For each exposure time, a corresponding dark image was taken and subtracted from the scientific images. The resulting image quality proved sufficient for this experiment.

### 3.2. Experimental protocol

#### 3.2.1. Adjustment of pupil size

The focal mask is removed from the beam and the camera is located in pupil plane E. A wide Lyot stop aperture is chosen in order to observe the entrance pupil. The iris P1 is adjusted to the desired size as measured off the TV monitor, see Fig. 4a. As the focal mask is replaced in the beam, the pupil image is transformed, rejecting light into a halo surrounding the geometrical pupil, see Figs. 4b–d, corresponding to the mask radii of  $0.455 \lambda/D$ ,  $0.516 \lambda/D$  and  $0.741 \lambda/D$ , respectively. The efficiency of this rejection and the distribution of the residual intensity within the pupil depends upon the size of the entrance iris. The Lyot stop iris P2 is now closed down so as to eliminate the bright halo, leaving only the residual light within the geometrical pupil. To account for mis-alignments and scatter, the Lyot pupil must always be slightly smaller than the entrance pupil.

#### 3.2.2. Image acquisition

The camera is now slid forwards to the image plane D and the coronagraph mask is removed in order to observe the non coronagraphic image. Camera exposure time is adjusted to the

minimum (0.04 ms), and a variable neutral density (ND) filter is adjusted so as to just avoid saturation of the PSF peak. Images are then acquired at 0.04 ms, 4 ms and 400 ms, in order to constitute a fiducial reference image, see Fig. 5a. The exact pupil size is deduced from comparing this image with a theoretical Airy pattern.

The coronagraphic mask is then placed in the beam and carefully centered to optimize symmetry in the coronagraphic image. Again a series of images is taken, the first one with an exposure time adjusted to just avoid saturation without changing the ND filter, then one or two more images with exposure times ranging up to the maximum allowable of 1 s. Figures 5b–d show composite images for the same three mask radii as considered above.

## 4. Experimental results

### 4.1. Results in the pupil plane

The key to understanding the Roddier & Roddier coronagraphic principle lies in the pupil plane. Simple Fourier optics allows us to appreciate the nulling effect due to the beam diffracted by the coronagraphic mask, shifted  $\pi$  radians out of phase, as it interferes with the original top-hat pupil. Since the phase mask is smaller than the stellar Airy pattern, the diffracted beam is broader than the original pupil and it extends beyond the geometrical pupil and since the mask is hard-edged, we expect to see diffraction rings.

Figures 6a–c compare the theoretical coronagraphic intensity profiles in the coronagraph exit pupil plane C with the experimental intensity profiles in the same plane. Again, the images correspond to the mask radii considered above, of respectively  $0.455 \lambda/D$ ,  $0.516 \lambda/D$  and  $0.741 \lambda/D$ .

The measured profiles compare well with the theoretical predictions, and the dark diffraction ring is clearly seen. Inside the pupil, the intensity falls sharply, indicating the destructive interference due to the good matching of the field strength of the diffracted beam phase shifted by  $\pi$  radians and the undiffracted beam. For the larger mask, the residual is stronger, but well apodized as expected.

### 4.2. Results in the image plane

Azimuthally averaged profiles of the coronagraphic and non coronagraphic images have been calculated, see Figs. 7a–c. The non coronagraphic profile is compared with the theoretical Airy pattern, indicating a very good correspondence. This comparison turned out to be useful in optimizing the image analysis approach, allowing to understand some unexpected features of the camera such as exposure-time saturation for the shortest exposure times, leading us to implement a non-linear exposure-time correction. Theoretical coronagraph images were calculated using the semi-analytic method based on matrix Fourier transforms described by Soummer et al. (2007).

In order to investigate the effect of varying mask size, we have calculated the intensity at different distances from the star, plotted as a function of mask radius, both for theoretical and measured profiles. Figure 8 displays these results. We considered six distances from the main optical axis, corresponding to the central peak and the first five bright rings of the Airy diffraction pattern (see Table 1). At each of these positions, we averaged the intensity of the coronagraphic image over an annulus of width  $\lambda/D$ . Theoretical results are plotted as lines, and experimental data are plotted as points. All results are normalized with respect

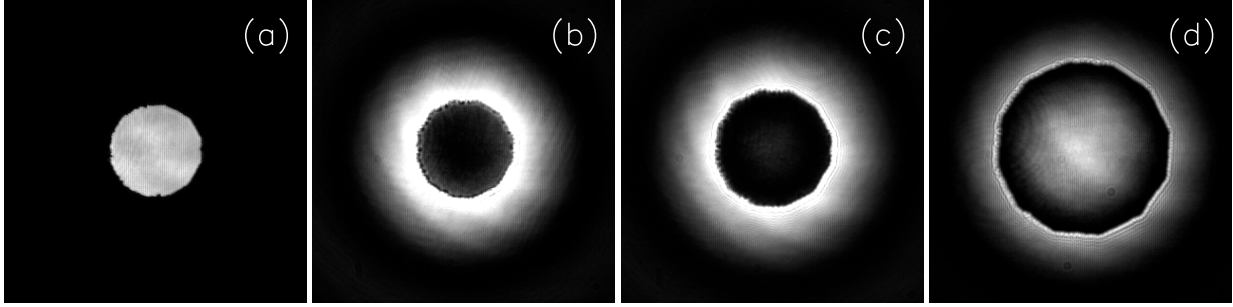


**Fig. 4.** Set of pictures obtained in the pupil plane E. **a)** Non coronagraphic exit pupil image. **b), c)** and **d)** coronagraphic exit pupil images without Lyot stop corresponding to the mask radii of  $0.455 \lambda/D$ ,  $0.516 \lambda/D$  and  $0.741 \lambda/D$ , respectively.

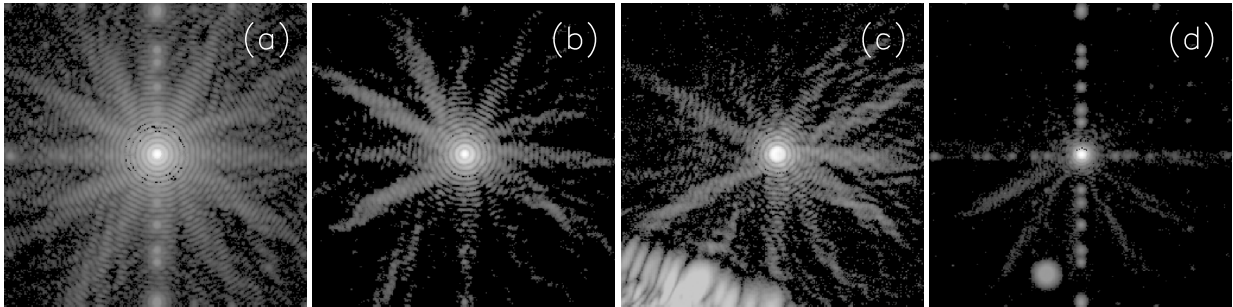


**Fig. 5.** Reconstructed images thanks to pictures taken in the image plane D at different exposure times. All the images are normalized to the peak of the non coronagraphic image. The gray scale is logarithmic, ranging from 1 (white) to  $10^{-7}$  (black). **a)** non coronagraphic image. **b), c)** and **d)** coronagraphic images with Lyot stop corresponding to the mask radii of  $0.455 \lambda/D$ ,  $0.516 \lambda/D$  and  $0.741 \lambda/D$ , respectively.

**Table 1.** Angular separations of the intensity peak and first five bright rings of the Airy diffraction pattern.

	Intensity peak	1st bright ring	2nd bright ring	3rd bright ring	4th bright ring	5th bright ring
Angular separation in $\lambda/D$	0.00	1.64	2.68	3.70	4.71	5.71

to the central intensity of the non coronagraphic image, averaged in the same way.

The theoretical curves clearly show that the mask giving the optimal peak attenuation, seen here to reach beyond  $10^4$ , does not correspond to the optimal performance in terms of contrast in the field. At the 5th Airy ring, an improvement by a factor of about 10 can be expected by increasing the mask radius to around  $0.65 \lambda/D$ . The experimental measurements confirm this result in spite of some loss of performance in the case of larger mask sizes. The coronagraphic PSF profiles in Fig. 7 indicate good correspondence with predictions down to a contrast of around  $10^{-6}$ , both for the  $0.455 \lambda/D$  mask (Fig. 7a) and the  $0.516 \lambda/D$  case (Fig. 7b). For the  $0.741 \lambda/D$  case (Fig. 7c), however, the correspondence with theory is less good. Still, the contrast performance in the field is clearly better than in the other cases. The same tendency is seen in Fig. 7, showing a loss in contrast of up to 1.7 mag for the larger masks.

Stray light present during our laboratory tests is probably responsible for much of the differences observed here. We have identified two main sources of such stray light: ghosts and surface scatter. Ghosts observed along the vertical and horizontal axis are clearly responsible for the large deviations from predictions at  $10\text{--}15 \lambda/D$  in Fig. 7c. However, they do not allow us to explain the difference observed at smaller distances from the optical axis. The most probable source of this discrepancy is scatter from optical surfaces. As stated in Sect. 3.1, we increase the pupil diameter in order to reduce the diffraction disk, hence

simulate larger mask diameters. Working with larger pupil diameters leads to more scattered light, hence reduced contrast, in the focal plane. Scatter from high-frequency roughness of the mask substrate is unlikely to contribute significantly to stray light in our system thanks to its sub-nanometric level (see Sect. 2) and since such stray light would be scattered outside of the Lyot stop.

Sampling problems are another likely contributor to the observed discrepancy. Enlarging the pupil diameter leads to a reduction of the size of PSF features, eventually becoming small compared with the detector dimension. The image smearing due to the convolution of the image with the detector pixels, combined with the presence of steep slopes in the image, can therefore be expected to result in a reduced image contrast as the apparent mask size increases.

#### 4.3. Effects of the RRPM on an off-axis source and residual tilt

While our experimental efforts have been concentrated on the behavior of the RRPM in the presence of an on-axis point source, it is also important to evaluate the coronagraphic effects on off-axis sources, i.e., circumstellar objects. This appears particularly important in view of one of the features of our results, indicating that what appears to be optimal mask dimensions for the classical RRPM has a considerably widened residual central peak. We wonder to what extent this widening affects the angular distance at which off-axis objects can be detected, and whether

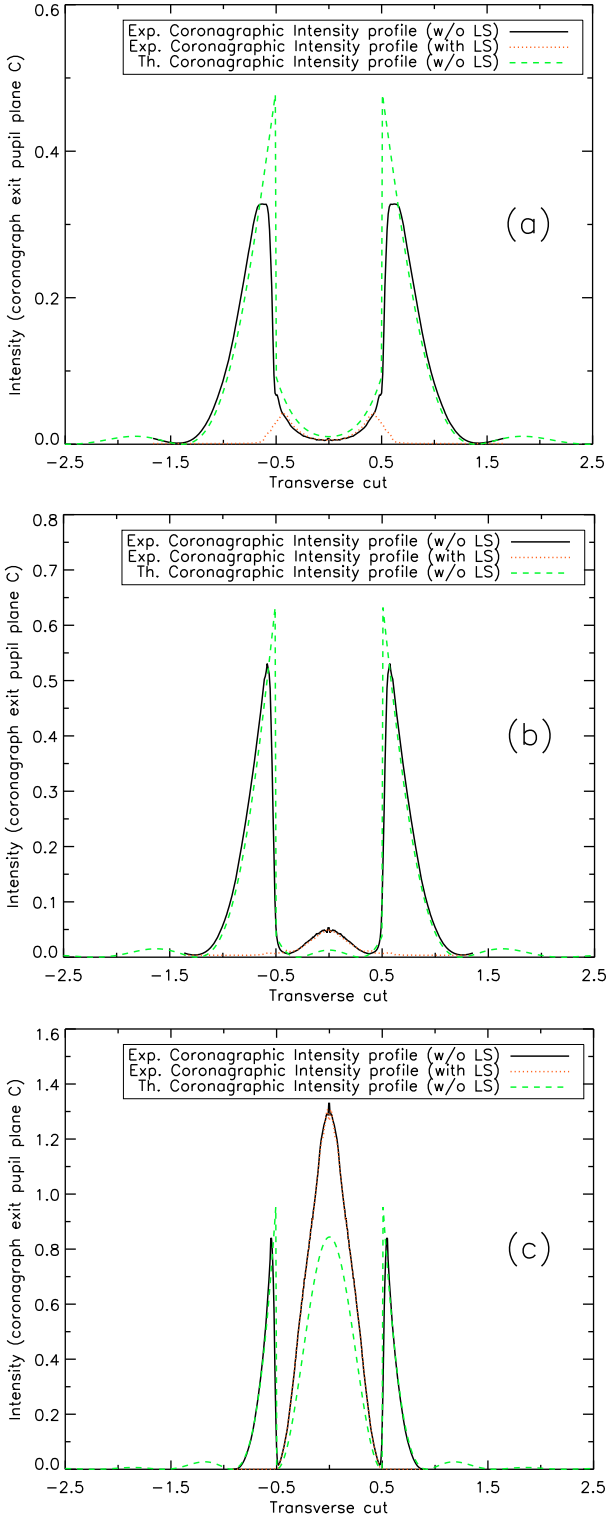


**Fig. 6.** Experimental and theoretical intensity profiles achieved in the re-imaged pupil plane C in the presence of the RRPM. Mask radii are estimated to be  $0.455 \lambda/D$  **a**),  $0.516 \lambda/D$  **b**) and  $0.741 \lambda/D$  **c**), respectively. LS stands for Lyot stop. See text for a detailed description of the plot.

off-axis objects also become wider. It is also interesting to investigate the sensitivity of this coronagraph to misalignment errors. To provide answers to these questions, we simulated a set of coronagraphic frames for different source locations:  $0.05 \lambda/D$ ,  $0.10 \lambda/D$ ,  $0.25 \lambda/D$ ,  $0.50 \lambda/D$ ,  $0.63 \lambda/D$ ,  $0.75 \lambda/D$ ,  $1.00 \lambda/D$ ,

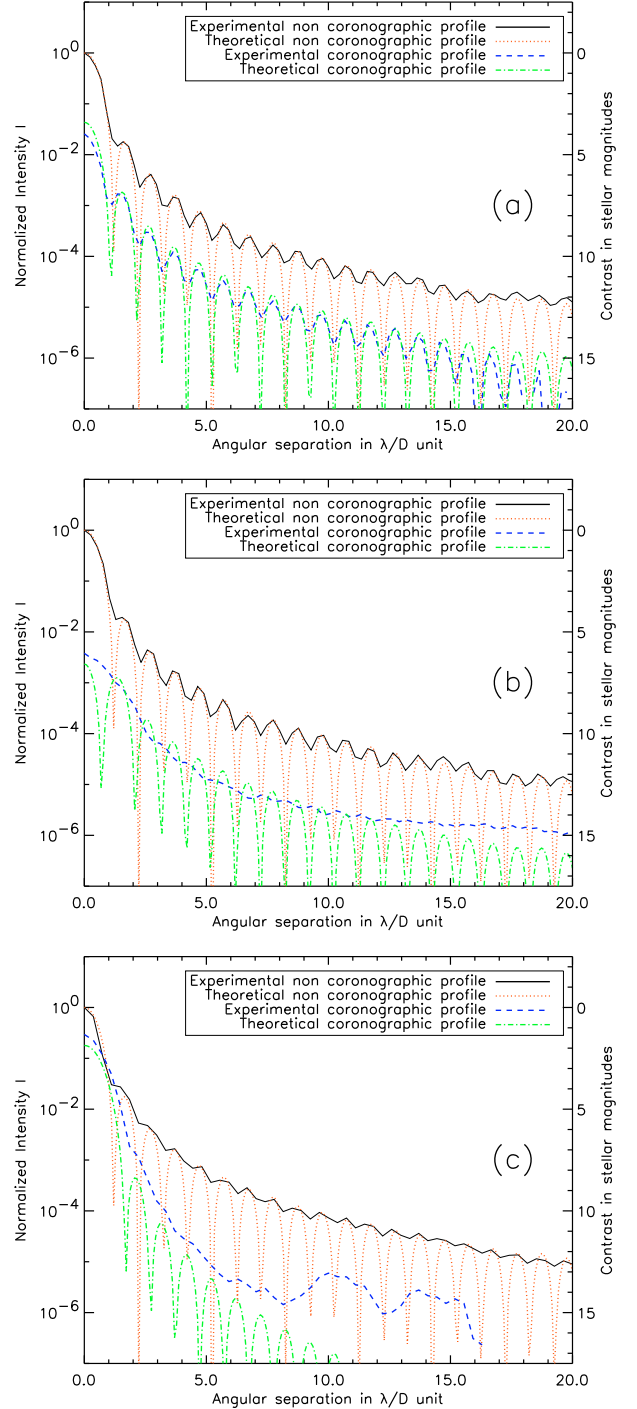


**Fig. 7.** Radial profiles of the experimental and theoretical images achieved in the presence or not of the RRPM. Mask radii are estimated to be  $0.455 \lambda/D$  **a**),  $0.516 \lambda/D$  **b**) and  $0.741 \lambda/D$  **c**), respectively.

$1.64 \lambda/D$  and  $2.68 \lambda/D$ , see Fig. 9. The smallest separations allow us to evaluate the sensitivity of the RRPM performance in the presence of alignment errors. The last two values, corresponding to the angular radii of the first and second Airy bright rings, allow us to determine how the shape and intensity of a possible stellar companion is affected by the RRPM. The mask radii are the same as the ones used to illustrate the experimental results, respectively  $0.455 \lambda/D$ ,  $0.516 \lambda/D$  and  $0.741 \lambda/D$  plus an intermediate value  $0.645 \lambda/D$ . In Figure 9, the left-hand column

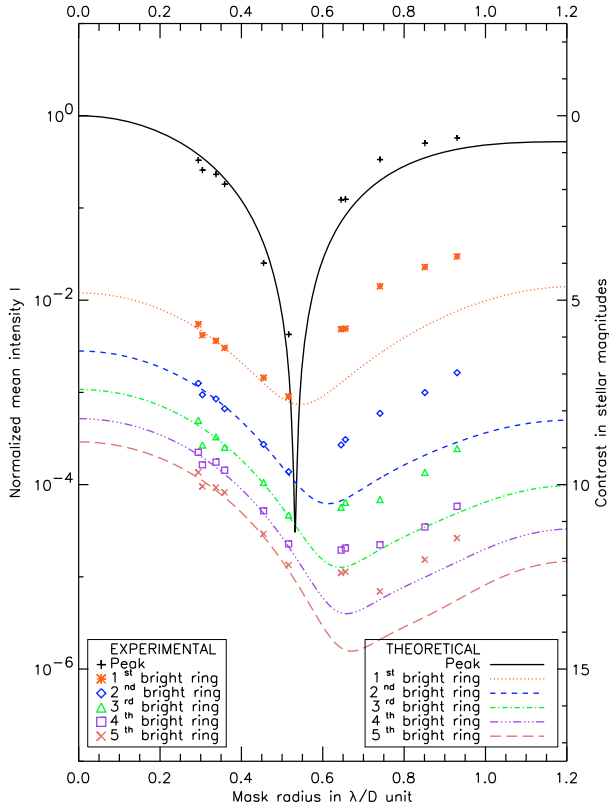


**Fig. 8.** Normalized image plane intensity at different field positions as a function of RRPM radius. The field positions considered correspond to bright rings in the non coronagraphic image, whose radial distances from the central star are given in Table 1. Theoretical intensities are shown as lines, experimental values are shown as points. See text for a detailed description of this plot.

represents an on-axis point source, and the bottom row represents non coronagraphic images.

The sensitivity to misalignment is clearly observed in the case of the larger ( $0.741 \lambda/D$ ) mask, for which the highest contrast is achieved. Contrast at a few  $\lambda/D$  from the star is perceptibly reduced for misalignments as small as  $0.05 \lambda/D$ . Curiously, however, this contrast reduction is not uniform across the field, and a dark, fringe-like zone can be observed on the right-hand side of the image. It is interesting to note that the contrast within this zone appears to reach very high levels. Further investigation of this phenomenon and its possible use to scan the inner zone of the stellar environment is outside the scope of this paper and will be the object of future work. The dark fringe moves inwards as the object moves outwards, and they coincide at about  $0.50 \lambda/D$  where the intensity at the source position falls to zero, see Fig. 10. As can be clearly seen in the image corresponding to a  $0.25 \lambda/D$  offset, this zone represents the limit between the coronagraphic PSF with a broadened central peak and the conventional PSF. This image also clearly shows that the coronagraphic PSF for this mask size has dark and bright diffraction rings inverted with respect to the conventional PSF, as is also seen in the PSF plots of Fig. 7. For larger offsets, the PSF rapidly becomes similar to the non-coronagraphic PSF, with the exception of a small anomaly at the position of the mask.

Other mask sizes show less spectacular effects of decentering, both in terms of contrast loss and in terms of PSF modification, but in the case of the  $0.516 \lambda/D$  mask, for which the central core of the coronagraphic PSF is narrower than the conventional PSF core, the off-axis PSF again recovers its usual core

dimension at around  $0.25 \lambda/D$ . Figure 10, showing normalized intensity at the source position as a function of source offset for different mask sizes, indicates that 50% transmission of the off-axis object is reached at around 1.3 to 1.4 times the mask radius. For the  $0.741 \lambda/D$  mask, this distance, commonly referred to as the inner working angle (IWA) equals  $1.035 \lambda/D$ .

## 5. Discussion and conclusion

The main goal of our experiment, demonstrating that improved technology was capable of providing a significant improvement of coronagraphic performance compared with the original RRPM demonstrator of 1999, has clearly been reached. In particular, while the original experiment was limited to a peak attenuation of 16, we have measured attenuation as high as 216. It is believed that the main improvement is in the mask profile, where our device has been seen to have a very sharp edge.

We have also provided a quantitative evaluation and experimental demonstration of the apodizing effect expected for larger phase masks, as described by Ferrari et al. (2007), in spite of a deterioration of the experimental results for mask radii larger than  $0.55 \lambda/D$ . We believe the main reasons for this deterioration are linked to features of our experimental setup, combined with the high peak intensity and increased aperture size corresponding to the larger mask diameters. In particular, a family of ghosts are observed along the vertical axis, probably due to internal reflections between the detector surface and the double detector window. These ghosts are invisible in the case of the small masks (Figs. 5b and c), but are clearly seen both in the non-coronagraphic image (Fig. 5a) and in the large-mask coronagraphic image (Fig. 5d). Deficiencies in terms of optical quality of the bench also become more important in the case of the larger mask size, where the entrance pupil was enlarged so as to reduce the focal ratio. This stresses the optical setup both in terms of source uniformity, optical aberrations, and surface quality. Other error sources include mechanical stability and adjustment accuracy. All adjustments are manual, with direct TV images as the only aid to alignment. Slight misadjustments cause spillage of light back into the pupil, hence reduced coronagraphic efficiency.

Thanks to this technological demonstration, we believe the RRPM, especially in its apodized version expected to act as a perfect monochromatic coronagraph (Guyon & Roddier 2000; Aime et al. 2002; Soummer et al. 2003a), could find its place in astrophysical instruments when spectral bandwidth can be traded off against access to small inner working angles. It can also be used as a tool for experimental studies of coronagraphic imaging: our bench has already served this purpose, demonstrating the effect of dust and cosmetic defects in high contrast imaging systems (Dohlen 2008). Furthermore, our results clearly pave the way for the achromatic Dual Zone coronagraph (Soummer et al. 2003b). A more elaborate version of our bench is currently being prepared where we plan to implement an apodized version of the RRPM coronagraph, as well as a prototype DZPM coronagraph which is being developed for the E-ELT study.

*Acknowledgements.* We are grateful for a grant from the Grupo Santander (Spain) through Encuentros Astrofísicos Blas Cabrera (UNAM-IAC), and our home institutions for their support. M. N'Diaye was supported by a scholarship from the Foreign Office of the Mexican Government and a grant from the Foreign Office of the French Government through the EGIDE organism. The authors would like to thank the anonymous referee for her/his helpful comments and suggestions which allow us to greatly improve the present paper.

**Table 2.** Averaged difference between the experimental and theoretical intensity values for different mask radii.

Mask radius in $\lambda/D$	0.294	0.304	0.338	0.359	0.455	0.516	0.645	0.656	0.741	0.851	0.930
$\Delta I$ in stellar magnitudes	0.12	0.21	0.06	0.07	0.07	0.09	1.67	1.72	1.54	1.54	1.66

We exclude the central peak values from the averages.

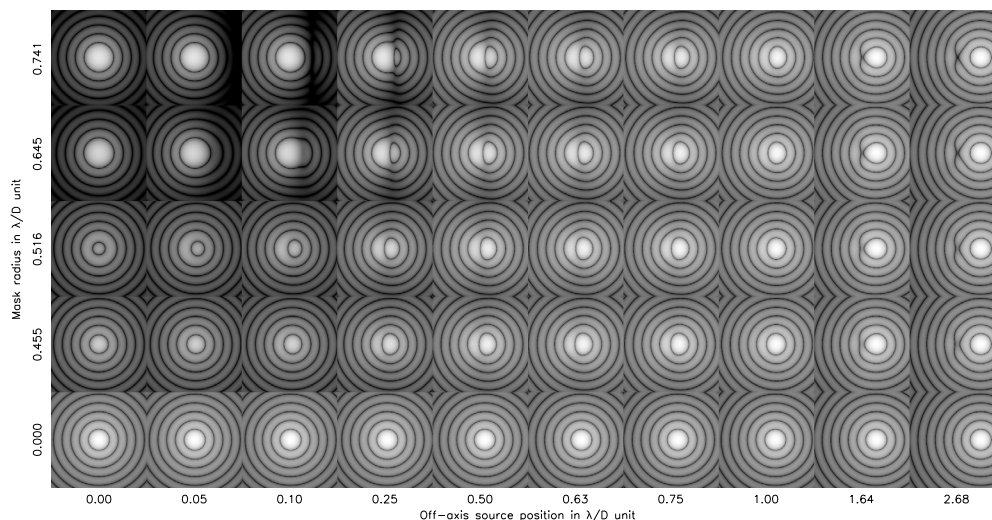


**Fig. 9.** Set of non coronagraphic and coronagraphic images computed numerically for different off-axis source positions and RRPm radii. All the images are normalized to the peak of the non coronagraphic image. The gray scale is logarithmic, ranging from 1 (white) to  $10^{-7}$  (black). The pixel scale is the same for all the images and the field of view is represented with a linear range of  $11 \lambda/D$ .

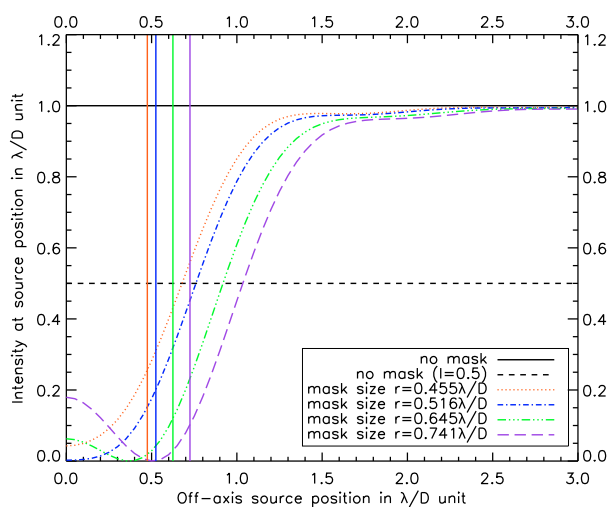


**Fig. 10.** Normalized coronagraphic image intensity at the source position as a function of the off-axis source position in the field and for different RRPm radii. The mask radius is indicated by the vertical lines.

## References

Aime, C., & Soummer, R. 2004, *ApJ*, 612, L85  
Aime, C., Soummer, R., & Ferrari, A. 2002, *A&A*, 389, 334  
Baudoz, P., Boccaletti, A., Riaud, P., et al. 2006, *PASP*, 118, 765  
Beuzit, J.-L., Feldt, M., Dohlen, K., et al. 2006, *The Messenger*, 125, 29  
Boccaletti, A., Riaud, P., Baudoz, P., et al. 2004, *PASP*, 116, 1061  
Burrows, A., & Sharp, C. M. 1999, *ApJ*, 512, 843  
Dohlen, K. 2004, in *EAS Publications Series*, ed. C. Aime, & R. Soummer, 12, 33

Dohlen, K. 2008, in *SPIE Conf. Ser.*, 7017  
Dohlen, K., Langlois, M., Lanzoni, P., et al. 2006, in *SPIE Conf. Ser.*, 6267  
Ferrari, A., Soummer, R., & Aime, C. 2007, *Comptes Rendus Physique*, 8, 277  
Goodman, J. W. 1996, *Introduction to Fourier Optics*, 2nd edn. (New York, MA: The McGraw-Hill companies), 0  
Gratadour, D., Rouan, D., Boccaletti, A., Riaud, P., & Clénet, Y. 2005, *A&A*, 429, 433  
Guyon, O., Roddier, C., Graves, J. E., et al. 1999, *PASP*, 111, 1321  
Guyon, O., & Roddier, F. J. 2000, in *Interferometry in Optical Astronomy*, ed. P. J. Lena, & A. Quirrenbach, *Proc. SPIE*, 4006, 377  
Hodapp, K. W., Suzuki, R., Tamura, M., et al. 2008, in *SPIE Conf. Ser.*, 7014  
Kasper, M. E., Beuzit, J.-L., Verinaud, C., et al. 2008, in *SPIE Conf. Ser.*, 7015  
Macintosh, B., Graham, J., Palmer, D., et al. 2006, in *Advances in Adaptive Optics II*, ed. B. L. Ellerbroek, & D. Bonaccini Calia, *Proc. SPIE*, 6272, 62720L  
Marley, M. S., Gelino, C., Stephens, D., Lunine, J. I., & Freedman, R. 1999, *ApJ*, 513, 879  
Mawet, D., Riaud, P., Baudrand, J., et al. 2006, *A&A*, 448, 801  
Racine, R., Walker, G. A. H., Nadeau, D., Doyon, R., & Marois, C. 1999, *PASP*, 111, 587  
Riaud, P., Boccaletti, A., Rouan, D., Lemarquais, F., & Labeyrie, A. 2001, *PASP*, 113, 1145  
Riaud, P., Boccaletti, A., Baudrand, J., & Rouan, D. 2003, *PASP*, 115, 712  
Roddier, F., & Roddier, C. 1997, *PASP*, 109, 815  
Rouan, D., Riaud, P., Boccaletti, A., Clénet, Y., & Labeyrie, A. 2000, *PASP*, 112, 1479  
Sivaramakrishnan, A., Koresko, C. D., Makidon, R. B., Berkefeld, T., & Kuchner, M. J. 2001, *ApJ*, 552, 397  
Soummer, R., Aime, C., & Falloon, P. E. 2003a, *A&A*, 397, 1161  
Soummer, R., Dohlen, K., & Aime, C. 2003b, *A&A*, 403, 369  
Soummer, R., Pueyo, L., Sivaramakrishnan, A., & Vanderbei, R. J. 2007, *Optics Express*, 15, 15935  
Traub, W., Shaklan, S., & Lawson, P. 2007, in *In the Spirit of Bernard Lyot: The Direct Detection of Planets and Circumstellar Disks in the 21st Century*, ed. P. Kalas  
Woolf, N. & Angel, J. R. 1998, *ARA&A*, 36, 507